SUPPORTING INFORMATION

Mazzolini et al. 10.1073/pnas.1423162112

The phototransduction machinery in the rod outer segment has a strong efficacy gradient

Monica Mazzolini[a,b,1], Giuseppe Facchetti[a,1], Laura Andolfi[b], Remo Proietti Zaccaria[c], Salvatore Tuccio[c], Johannes Treu[d], Claudio Altafini[a,3], Enzo Di Fabrizio[e,f], Marco Lazzarino[b,g], Gert Rapp[d] and Vincent Torre[a,2]

a- International School for Advanced Studies (SISSA) via Bonomea 265, 34136 Trieste (Italy)
b- Cluster in Biomedicine S.c.r.l., Area Science Park, Basovizza, 34149 Trieste (Italy)
c- Istituto Italiano di Tecnologia (IIT), via Morego 30, 16163 Genova (Italy)
d- Rapp OptoElectronic GmbH, Branch Wedel Kronskamp 110, 22880 Wedel, (Germany)
e- King Abdullah University of Science and Technology (KAUST) Thuwal, 23955-6900 (Kingdom of Saudi Arabia)
f- Bio-Nanotechnology and Engineering for Medicine, Department of Experimental and Clinical Medicine, University of Magna Graecia 88100 Catanzaro, Italy
g- Istituto Officina dei Materiali - Consiglio Nazionale delle Ricerche, Basovizza, Area Science Park, 34149 Trieste (Italy)
1- Equally contribution.
2- To whom correspondence should be addresses. Email:torre@sissa.it
3- present address: Linkoping University, Sweden Dep. of Electrical Engineering Division of Automatic Control.

Table of contents:

Supplementary Text: MATHEMATICAL MODELLING

By using apertureless TOFs we were able to deliver localized spots of light at any flash intensity. Therefore we could measure photoresponses at different locations along the OS at the single photon level, dim and saturating light intensities. From these experiments we noticed that:

1. a single photon absorbed at the base and at the middle of the outer segment (OS) evokes detectable photoresponses, but not when it is absorbed at the tip (i.e. the response is lower than the noise);
2. The amplitude of photoresponses evoked by the same dim light decreases moving the TOF from the base to the tip (Fig.4A-C);
3. The maximal amplitude of photoresponses saturates (i.e. it does not increase when the light intensity increases) to a value which decreases moving from the base to the tip (Fig. 4D);
4. The saturation concerns both the maximal amplitude and the slope of the rising phase of the response (linear relationship between the two, see Fig.6F-G);
5. The saturation time (i.e. the time needed before the current starts to decrease from the saturating amplitude) does not increase when the light intensity increases (as it does, instead, in case of diffuse light, see Fig. 6E).

As explained in the following, these experimental observations suggested that:

- depletion of PDE along the OS is the most likely explanation for the observed efficacy gradient: both the saturation of the amplitude of the response and the gradient of efficacy can be explained by this hypothesis.
- the diffusion coefficient of cGMP in the cytoplasm is high and its value is consistent with what reported in literature.

A) Depletion of PDE as a possible explanation of the efficacy gradient along the OS.

We explain here in more details the theoretical modeling and the supporting experimental observations. We looked for a limiting factor explaining both kind of saturations observed with restricted spots of light. Possible candidates were the concentration of the compounds and the kinetics of the signaling pathway: these quantities could change moving from the base to the tip of the OS. Therefore, we considered one by one all these factors:

CyclicGMP: because of its fast diffusion in the cytoplasm and since it is continuously resynthetized, we excluded cyclicGMP.

Calcium and Guanylate Cyclase: the gradient of efficacy is already evident during the rising phase of the photocurrent (Fig. 6F) i.e. before the intervention of the feedback. For this reason we excluded the Guanylate cyclase and calcium dynamics.

CNG channels: It is known that CNG channels are uniformly distributed along the OS (1, 2, 3). Therefore their concentration cannot be the limiting factor in the cascade. We can also exclude the possibility of having CNG channels with a higher conductance at the base with respect to the rest of the OS (the kinetic feature), because patch-clamp recordings show that also the conductance of native CNG channels is homogenous along the OS (See Fig. S7).
We have considered the possibility that the observed efficacy gradient of the phototransduction machinery is caused by a gradient in the phosphorylation state of the CNG channels. Indeed as shown by Krajewskijl (4), phosphorylation of CNG channels decreases the sensitivity of these channels with respect to cGMP, so that their open probability will be lower. In this case, despite an homogeneous density of CNG channels along the rod OS (ROS) and a similar single channel conductance of CNG channels along the OS (our Fig. S7), the dark current entering into the tip of ROS will be lower than that entering into the base of ROS. However, as reported in the Baylor et al

(Ref. 5, Fig. 6) experiments on *Bufo marinus* rods reveal a linear increase of circulating dark current as a function of length of the OS drawn into the suction pipette. The length of OS in *Bufo marinus* is about 60 μm and in *Xenopus leavis* only 32 μm and it is easier to obtain an accurate relation between circulating dark current and the length of the OS sucked in *Bufo marinus* rods. In two experiments, we obtained similar results also in *Xenopus laevis* rods. Since with a saturating diffuse light all the CNG channels are closed, this linearity indicates that the density of dark current entering through the CNG channels is uniform along the OS. This observation and the fact that the density and the conductance of CNG channels are also uniforms, suggests that the fraction of open channels does not have any gradient along the OS. Consequently phosphorylation should not be responsible for the efficacy gradient we observed.
This conclusion is also supported by the following observation. We compared two non-saturating dim flashes, one at the base and one at the middle; because of the efficacy gradient, we used a weaker light intensity at the base in order to triggers the same maximal amplitude of the photocurrent obtained at the middle (see Fig. S8C). In this situation, if the CNG channels at the base have higher cGMP sensitivity, the amount of cGMP hydrolyzed at the base should be smaller than the amount hydrolyzed at the middle. Therefore, the time needed to re-synthesize all the cGMP (i.e. to recover the photocurrent to the baseline) would be longer at the base than at the middle. This is not observed in our experiments, as reported in Fig. S8C.

Rhodopsin and transducin: Rhodopsin is the most abundant protein on the surface of the internal disks: rhodopsin:transducin:PDE = 270:27:1 (Ref. 6) and its unlikely that it is responsible for the gradient of efficacy. Similarly transducin is rather abundant and availability of transducin cannot be considered as a limiting factor. We developed a simple mathematical model for the initial steps of the cascade before the intervention of the feedback (see Fig. S9A).
Because of its high concentration we assume that the amount of activated rhodopsin is proportional to the intensity I of the light stimulus ($[Rh^*]=\alpha I$). The dynamics of activated transducin (Gprotein, [G*]) and activated phosphodiesterase ([PDE*]) is described by the following equations (symbols according to Fig. S9A):

$$d[G^*]/dt = k\alpha I\,([G]_{tot}-[G^*]-[PDE^*])-\delta[G^*]-\beta[G^*]([PDE]_{tot}-[PDE^*])+\rho[PDE^*] \quad (S1)$$

$$d[PDE^*]/dt = \beta[G^*]([PDE]_{tot}-[PDE^*])-\rho[PDE^*] \quad (S2)$$

where $[G]_{tot}$ and $[PDE]_{tot}$ denote the total amount, in the illuminated area, of transducin and PDE, respectively. For a given intensity I, the slope $V(I)$ of the rising phase is defined as the maximal slope of the photoresponse A(t) after the stimulus. Therefore:

$$V(I) = \max dA/dt = \textit{proportional to } \max (d[CNG]/dt) = \max(d[CNG]/d[cGMP]\cdot d[cGMP]/dt). \quad (S3)$$

Since d[CNG]/d[cGMP] does not change along the OS (see previous paragraph "CNG channels") and we are always far from the complete closure of all the CNG channels, Eq. (S3) indicates that $V(I)$ is proportional to the maximal rate of hydrolysis of cGMP (d[cGMP]/dt), i.e. to the maximal amount of activated phosphodiesterase: therefore, by setting d[PDE*]/dt=0 we obtain:

$$[PDE^*]_{max} = \beta[G^*][PDE]_{tot} / (\beta[G^*]+\rho), \quad (S4)$$

which is maximal when also [G*] is maximal:

$$[G^*]_{max} = k\alpha I([G]_{tot} - [PDE^*])/ (k\alpha I + \delta) \approx k\alpha I[G]_{tot} / (k\alpha I + \delta), \quad (S5)$$

where the approximation can be justified by the fact that $[G]_{tot} >> [PDE]_{tot} > [PDE^*]$. Therefore, combining the two expressions and using the proportionality between $V(I)$ and $[PDE^*]_{max}$:

$$V(I) = V_{max}\, I / (I + K_s) \quad \text{(S6)}$$

where:

$$V_{max} = \beta[G]_{tot}*[PDE]_{tot} / (\beta[G]_{tot} + \rho) \quad \text{and} \quad K_s = \delta\,\rho / k\alpha(\beta[G]_{tot} + \rho). \quad \text{(S7)}$$

The fitting of the experimental data with Eq. (S6) for the illumination at the base, middle and tip of the OS gave the values of V_{max}= 27.7, 12.6, 2.5 pA/s, K_s=1080±80, 1100±170, 1100±500, respectively (see also Fig. S9B-C). K_s is almost constant and has a similar value along the OS, suggesting that all the kinetic parameters (activity and absorption capability of rhodopsin: k and α; activity of transducin: β; degradation rates: δ and ρ) and the total amount of transducin ($[G]_{tot}$) are the same at every position along the OS.
This result indicates that:

- the kinetics of the rhodopsin in the activation of transducin cannot justify the reduction of the efficacy along the OS (parameter k must be constant): indeed, if there is a gradient in the functionality of the rhodopsin, increasing the light intensity will counterbalance a lower rhodopsin functionality and the amplitude of photoresponses are expected to increase; this was not observed in our experiments (as example see Fig. 1D when passing from I to 2I);
- the migration of transducin to the inner segment (i.e. $[G]_{tot}$) can be excluded as reason for a lower efficacy at the tip. In order to exclude this hypothesis, we also performed experiments stimulating the base, the middle and the tip with different sequences of TOF position: no differences were observed and the same results were obtained stimulating first the base or the tip or the middle.

Consequently, the only remaining parameter which can justify the change of V_{max} is $[PDE]_{tot}$.

Phosphodiesterases: PDE is the least abundant protein among the three that are linked to the internal disc membrane and it is likely to be the correct candidate.
By restricting the model used for transducin to the PDE dynamics only, i.e.

$$d[PDE^*]/dt = k\alpha I([PDE]_{tot}-[PDE^*])-\rho[PDE^*] \quad \text{(S8)}$$

we obtain the same expression (S6) with:

$$V_{max} = [PDE]_{tot} \quad \text{and} \quad K_s = \rho / k\alpha. \quad \text{(S9)}$$

Also in this case $[PDE]_{tot}$ change along the OS while the kinetics parameters remain constant. Therefore, the fact that after doubling the light intensity there is no increase of the response amplitude is due to the limited amount of PDE in the illuminated part (PDEs saturate). In the case of diffuse light, instead, all the PDEs of the OS are involved and then the limiting factor will be the closure of all CNG channels caused by the complete hydrolysis of all cGMP molecules in the cytoplasm.

B) Constant saturation time from restricted illumination

The fact that PDE is the limiting factor in case of restricted illumination provides also an explanation of the saturation time (point 4). Fig. 6E of the main text shows that, the time by which photoresponses remain saturated increases by increasing the light intensity with diffuse illumination, but not with restricted spots of light. Because of its reduced availability, in case of restricted illumination only a small amount of PDE is activated also with saturating flashes. From

our previous model, this limited amount is responsible for both the slope of the rising phase and for the amplitude of the response. In contrast, in the case of diffuse light, the saturation is due to cGMP and CNG channels. The number of activated PDEs in the whole OS is indeed much higher that what is sufficient to close all the CNG channels. Therefore, with very bright diffuse lights, a "surplus" of PDEs is activated. The larger is this "surplus" (i.e. brighter is the light intensity), the longer will be the time necessary to decrease the number of activated PDEs below the level corresponding to the closure of all CNG channels. We quantify this idea with the following simple model.
Let $g(x,t)$ be the concentration profile of cGMP along the OS, $[CNG]_{close}$ the fraction of closed CNG channels and $A(t)$ the amplitude of the response. Using the same notation as in the previous sections, for a given light intensity I, the dynamics of $[PDE^*](t,I)$ can be described by the following expression (Ref. 7):

$$[PDE^*](t,T) = [PDE^*]_{max}(I)\ t\ \rho\ e^{(-\rho t-1)}, \qquad \text{(S10)}$$

where $[PDE^*]_{max}(I)$ can be obtained by the equation (S6) and is

$$[PDE]_{max}(I) = [PDE]_{tot}\ I\ /(\ K_s+I). \qquad \text{(S11)}$$

and $[PDE]_{tot}$ indicates the total number of PDE available in the illuminated area. Clearly we have:

$$[PDE]_{tot\ (DIFFUSE)} >> [PDE]_{tot\ (FIBRE)}. \qquad \text{(S12)}$$

For the regulation of the CNG channels we use the Hill equation (see for instance Ref. 8):

$$[CNG]_{close}(x,t) = H^2\ /\ [H^2 + g(x,t)^2], \qquad \text{(S13)}$$

Then, the photoresponse amplitude A(t) is:

$$A(t) = J \int_{[0,L]} [CNG]_{close}(x,t) - [CNG]_{close}(x,0)dx, \qquad \text{(S14)}$$

where L is the length of the OS and J is the CNG single channel current. The fraction of closed channels can be used to estimate the calcium feedback by the following equation:

$$feedback = b\ [CNG]_{close} = \varphi\ H^2\ /\ [H^2 + g(x,t)^2]. \qquad \text{(S15)}$$

Therefore, the dynamics of cGMP concentration is given by:

$$\partial g(x,t)/\partial t = D\ \Delta g(x,t) - k[PDE]_{tot}\ I\ /(I+K_s)\ t\ \rho\ e^{(-\rho t-1)} g(x,t) + \varphi\ H^2\ /\ [H^2 + g(x,t)^2] - \eta\ g(x,t) \qquad \text{(S16)}$$

where D and η are the diffusion coefficient and the spontaneous hydrolysis rate of cGMP, respectively. Using parameter values consistent with the literature (9, 10, 11), the simulated dynamics well reproduce the desired effect: the saturation time increases with the light intensity in case of diffuse illumination whereas it remains constant in case of restricted light (see Fig. S10).

C) Diffusion of cGMP

Localized illumination induces the generation of spatial gradient of cGMP along the OS. Therefore, we used the results obtained with a restricted illumination to estimate the diffusion coefficient of cGMP, D_{cGMP}. The cytoplasm was described as a stack of discs with a diameter d = 4 μm and length L = 32 μm (see Fig. S11A). We assume that cyclicGMP hydrolysis occurs only on the discs where PDEs have been activated. Since the efficacy of the cascade is maximal at the base, we

considered the rate of hydrolysis at the base to be very high, i.e. almost instantaneous. Due to radial symmetry, the 3D cylindrical geometry was reduced to a 2D domain where the Laplacian was expressed in cylindrical coordinates (with no angular coordinates). The equation for the cytoplasm was then the simple Fick's law equation:

$$\frac{\partial g(x,r,t)}{\partial t} = D_{cGMP}\left[\frac{1}{r}\frac{\partial}{\partial r}\left(r\frac{\partial g(x,r,t)}{\partial r}\right)+\left(\frac{\partial^2 g(x,r,t)}{\partial x^2}\right)\right], \quad \text{(S17)}$$

where the diffusion coefficient D_{cGMP} was the only free parameter. A schematics representation of the grid for the discretization is reported in Fig. S11B. The space between adjacent discs and the gap between disc perimeter and external membrane have been discretized as a sequence of concatenated nodes at 50 nm distance from each other (with the same distance between adjacent discs). In each node, Eq. (S17) holds. For the blue nodes (activated PDE) Dirichlet boundary conditions $g(x,r,t)=0$ was applied (because of the high efficiency of the phototransduction at the base). Neumann reflective boundary conditions ($\partial g(x,r,t)/\partial x=0$ or $\partial g(x,r,t)/\partial r=0$) were instead applied for the red and green nodes (because of a radial symmetry and because of an external membrane border, respectively). We solved numerically Eq. (S17) for t = [0, 500] ms (which is the time at the peak), starting from an initial condition of a uniform cGMP concentration equal to 3.5 μM. Since the time interval covers the initial part of the response, PDE in the illuminated discs is considered constantly active for the entire time interval.

The size of the illuminating spot (varying between 2 to 9 μm in diameter, see Fig. 2B-C) was translated into an equivalent number of discs with activated PDEs. In order to have a photoresponse reaching 52 ± 8% of the maximal photoresponse to diffuse light in these 500 ms (case of THw fiber, Fig. 2E), D_{cGMP} must be between 220-360 $\mu m^2/s$ (Fig. S11C red lines). These values were confirmed by the experiments with THn fiber: indeed, to reach 31 ± 3% (Fig. 2F) of the maximal photoresponse obtained with diffuse light, the range of the diffusion of cGMP was 230-300 $\mu m^2/s$ (Fig. S11C blue lines). Therefore our experiments with restricted spots of light, in agreement with previous analysis (9, 12, 13), indicate a high value of the intracellular diffusion for cGMP, with D_{cGMP} equal to 220 and 360 $\mu m^2/s$.

SI References

1. Baylor DA, Lamb TD, Yau KW (1979) Responses of retinal rods to single photons. *J Physiol* 288:613-634.

2. Watanabe S, Matthews G (1988) Regional distribution of cGMP-activated ion channels in the plasma membrane of the rod photoreceptor. *J Neurosci* 8(7):2334-2337.

3. Karpen JW, Loney DA, Baylor DA (1992) Cyclic GMP-activated channels of salamander retinal rods: spatial distribution and variation of responsiveness. *J Physiol* 448:257-274.

4. Krajewski JL, Luetje CW, Kramer RH (2003) Tyrosine phosphorylation of rod cyclic nucleotide-gated channels switches off Ca2+/calmodulin inhibition. *J Neurosci* 23(31): 10100-10106.

5. Baylor DA, Lamb TD, Yau KW (1979) The membrane current of single rod outer segments. *J Physiol* 288:589-611.

6. Pugh EN Jr, Lamb TD (2000) Phototransduction in vertebrate rods and cones: molecular mechanisms of amplification, recovery and light adaptation. *Handbook of Biological Physics*. (Elsevier, Amsterdam) pp 183–255.

7. De Palo G, Facchetti G, Mazzolini M, Menini A, Torre V, Altafini C (2013) Common dynamical features of sensory adaptation in photoreceptors and olfactory sensory neurons. *Sci Rep* 3:1251. doi: 10.1038/srep01251.

8. Caruso G, Bisegna P, Andreucci D, Lenoci L, Gurevich VV, Hamm HE, DiBenedetto E (2011) Identification of key factors that reduce the variability of the single photon response. *Proc Natl Acad Sci U S A* 108(19):7804-7807.

9. Koutalos Y, Nakatani K, Yau KW (1995) Cyclic GMP diffusion coefficient in rod photoreceptor outer segments. *Biophys J* 68(1):373-382.

10. Caruso G, Bisegna P, Shen L, Andreucci D, Hamm HE, DiBenedetto E (2006) Modeling the role of incisures in vertebrate phototransduction. *Biophys J* 91(4): 1192-1212.

11. Gross OP, Pugh EN Jr, Burns ME (2012) Spatiotemporal cGMP dynamics in living mouse rods. *Biophys J* 102(8): 1775-1784.

12. Nakatani K, Chen C, Koutalos Y (2002) Calcium diffusion coefficient in rod photoreceptor outer segments. *Biophys J* 82(2):728-739.

13. Gross OP, Pugh EN Jr, Burns ME (2012) Calcium feedback to cGMP synthesis strongly attenuates single-photon responses driven by long rhodopsin lifetimes. *Neuron* 76(2):370-382.

14. Marchesi A, Mazzolini M, Torre V (2012) Gating of cyclic nucleotide-gated channels is voltage dependent. *Nat Commun* 3:973 doi:10.1038/ncomms1972.

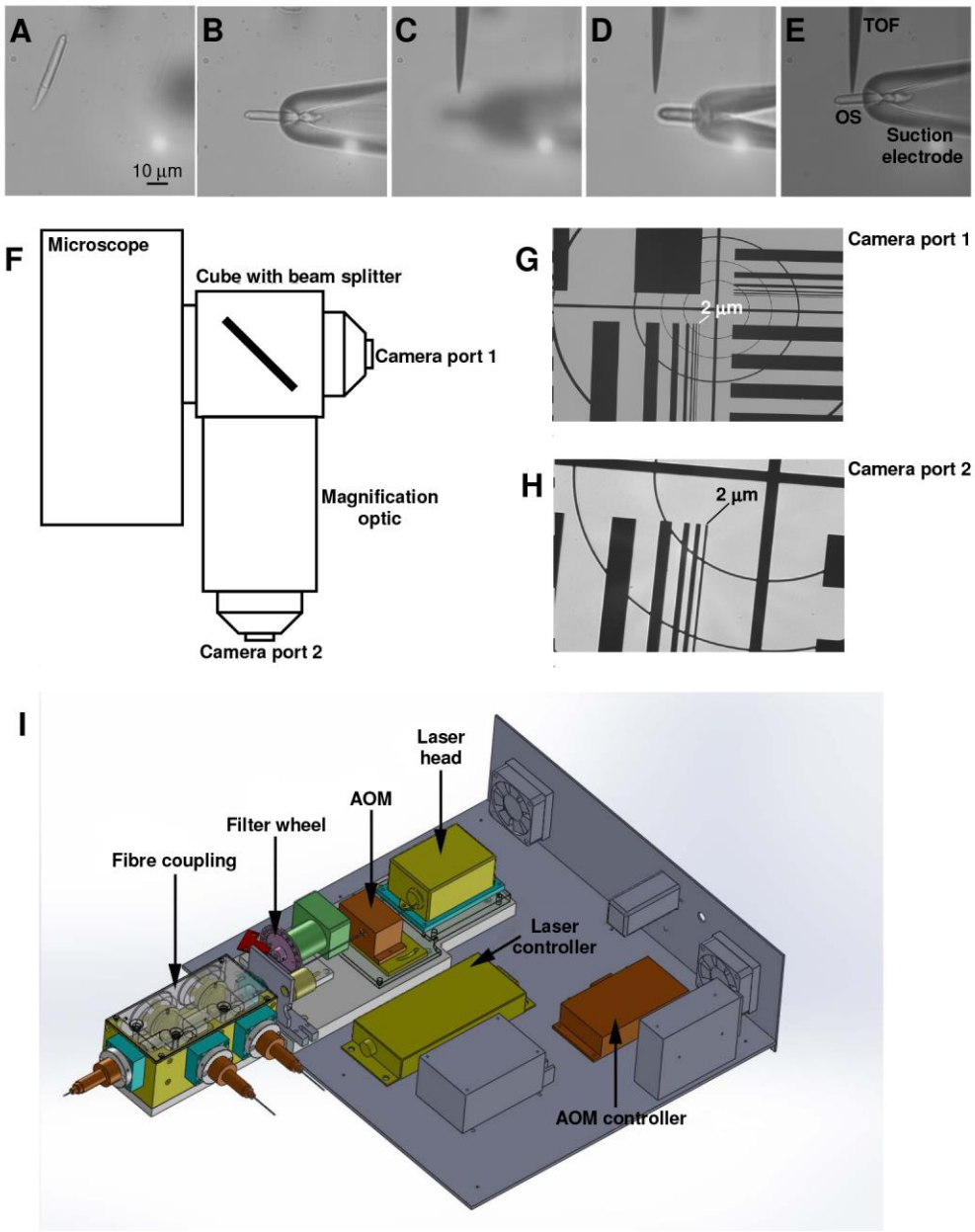

Fig. S1. Recording apparatus. In order to observe the samples with different magnifications without inducing vibrations by turning an objective revolver, we constructed a dual camera port with different magnification for each port. (A-E) The approach sequence between the rod and the TOF is subdivided in five steps; an isolated intact rod from the Xenopus laevis retina is visualized (A) and the IS is drawn into a suction pipette (B). Subsequently the TOF is imaged (C) and the suction pipette is moved towards it (D) and finally the OS is brought into physical contact with the TOF positioned at 90° touching it (E). All images were acquired using a Jenoptic camera under infrared light as described in the text. (F-I) Two cameras are mounted onto the side port of the microscope (F). Image of a test grid with 10x objective mounted on port 1 (G) and on port 2 with magnification optics (H). Size of camera field in panel (G): 860µm x 550µm, panel (H): 280µm x 180µm. The laser system (I) consisting of laser head, AOM, filter wheel, three ports for optical fibers and a micro controller. The laser power (100 mW) was distributed to the three ports using beam splitters. Each port with the TOF received 45% of the laser power whereas 10% of the power was directed to the port with a multimode fiber for diffuse illumination.

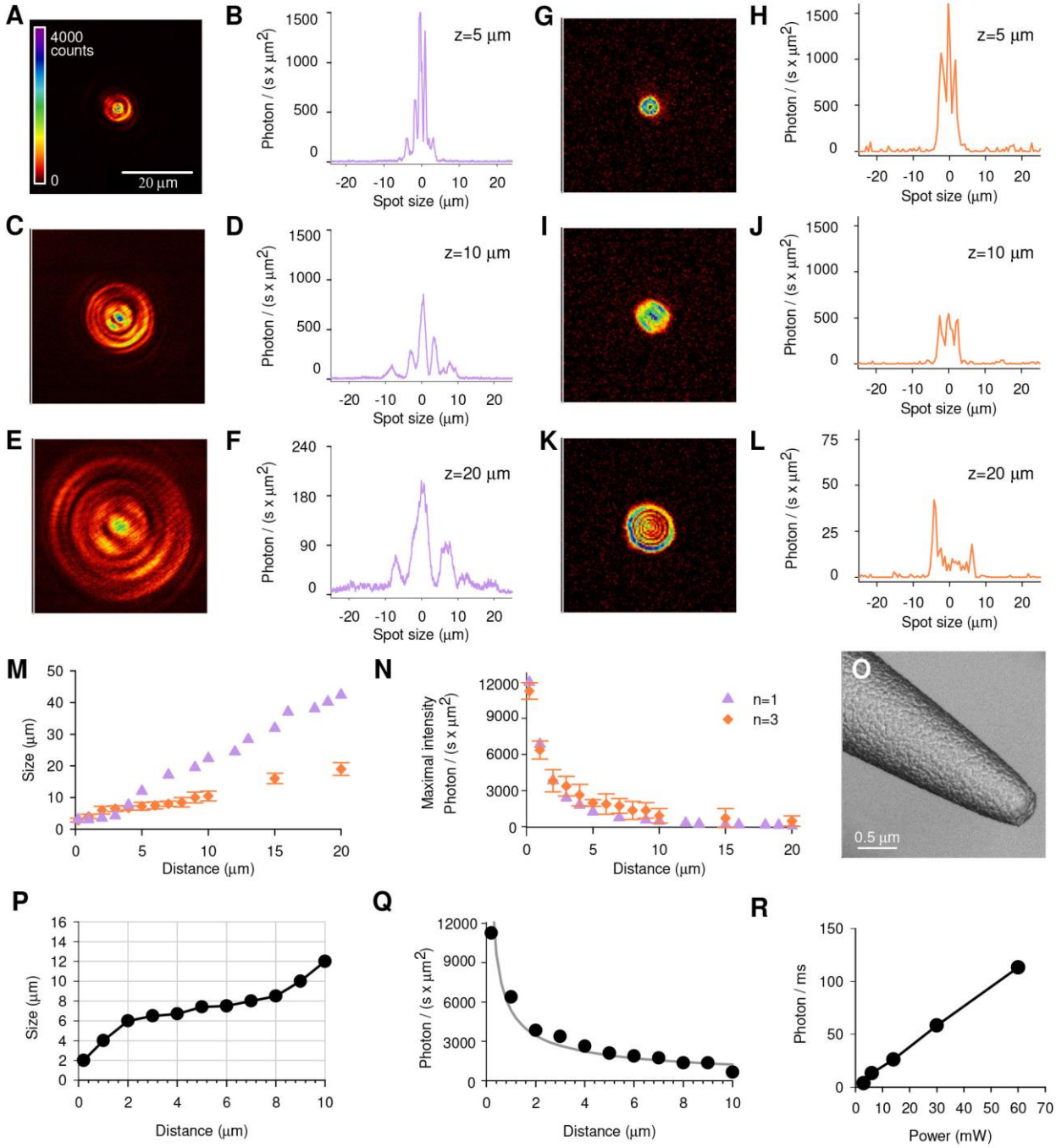

Fig. S2. Optical characterization of Bessel like and top-hat like TOFs. (A-F) Spatial two dimensional and lateral profile of light emitted by an apertureless Bessel-like TOF at z = 5, 10 and 20 µm fiber-sensor distance (violet). (G-L) Spatial two dimensional and lateral profile of light emitted by an apertureless Top-hat like TOF at z = 5, 10 and 20 µm fiber-sensor distance (orange). (M) Width of the light beam (measured as the width of the profile above the noise level) as a function of the distance from the TOF apex. (N) Relationship between the fiber-sensor distance and the maximal amplitude of the light intensity. Violet and orange symbols correspond to data from apertureless Bessel-like and top-hat like TOFs respectively as in panels (A-L). Data were expressed as the mean ± s.e.m. for n fibers. (O) Scanning electron microscope (SEM) image of an apertureless TOF. (P) The distance-size plot depicts the relation between the fiber-sensor distance and the dimension of the light spot (measured considering the noise threshold). (Q) The distance-maximal amplitude plot depicts the relation between the fiber-sensor distance and the maximal amplitude of the light intensity; the maximal light intensity decreases with the distance z as 1/z. (R) Calibration of the light intensity (volume of the wave-front profile) exiting from the TOF with respect to the power of the laser source.

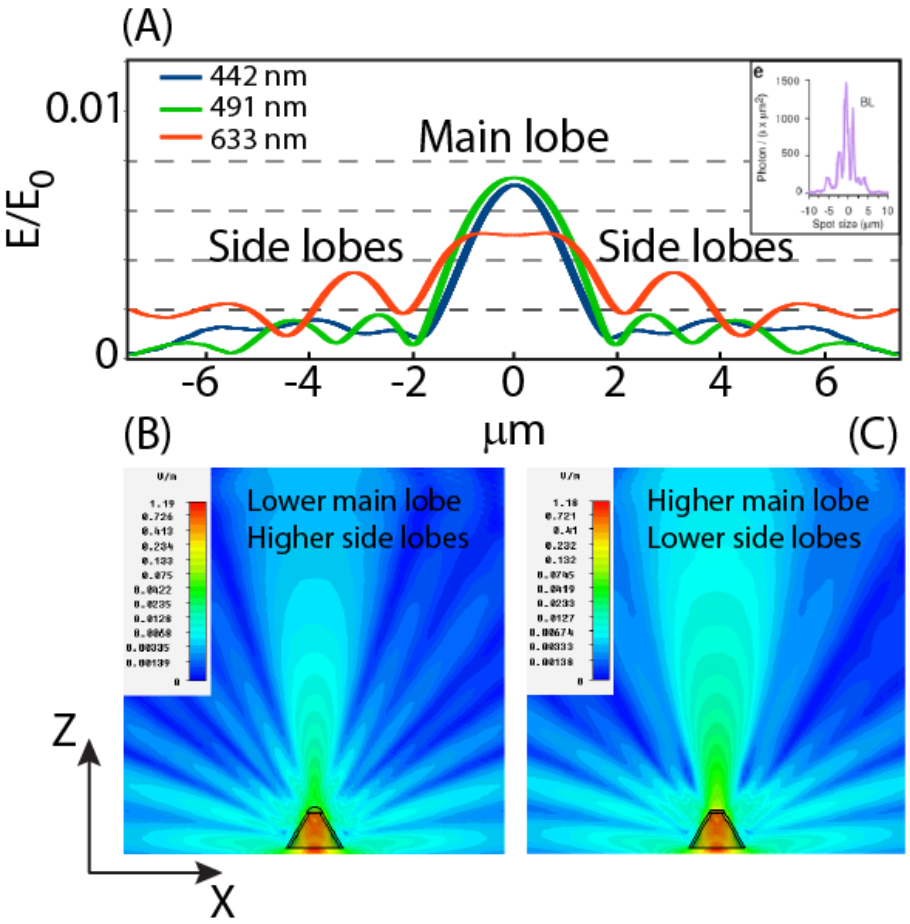

Fig. S3. Simulation of the light profile exiting from apertureless TOFs: Bessel like lateral profile. The figure shows the simulated 1D profile which best reproduces the data of Fig. 1E of the main text, referred as the truncated Bessel-like light profile. (A) 1D electric field (amplitude E/E_0) profiles representing the electric field at 5 µm from the tip apex. Three laser sources have been considered at a wavelength of 442 nm, 491 nm and 633 nm. While at 442 and 633 nm the exiting light show a similar behaviour, the 633 nm excitation results in an off-resonant condition with the fibre geometry. (B) 2D electric field map of the structure producing the 1D profile in (A) under 491 nm excitation. The total apex angle is equal to 60 degrees with an Au thickness, around the apex region, up to 200 nm. (C) 2D electric field map of a similar structure as (B) with Au apex thickness of 100 nm. Also in this case the excitation wavelength is 491 nm. Inset in (A): Fig. 1E of the main text. The structure generating truncated Bessel-like (BL) profiles is something in between the cut-edge and rounded structures. In fact, it is characterized by an increased Au thickness in the region around the tip apex (about 200 nm of gold) and by an apex angle of 60 degrees. These two factors together contribute to the realization of a profile similar to Fig. 1E in the main text. In fact, the increase of the apex angle is responsible of the axicon behaviour - producing both the main and side lobes - while the increase of the Au thickness around the tip apex region (from 100 nm to 200 nm) attenuates the main central lobe and enhances of the side lobe amplitude. By further optimizing the apex angle and the Au apex thickness, electric field profiles almost identical to those of Fig. 1E can be expected.

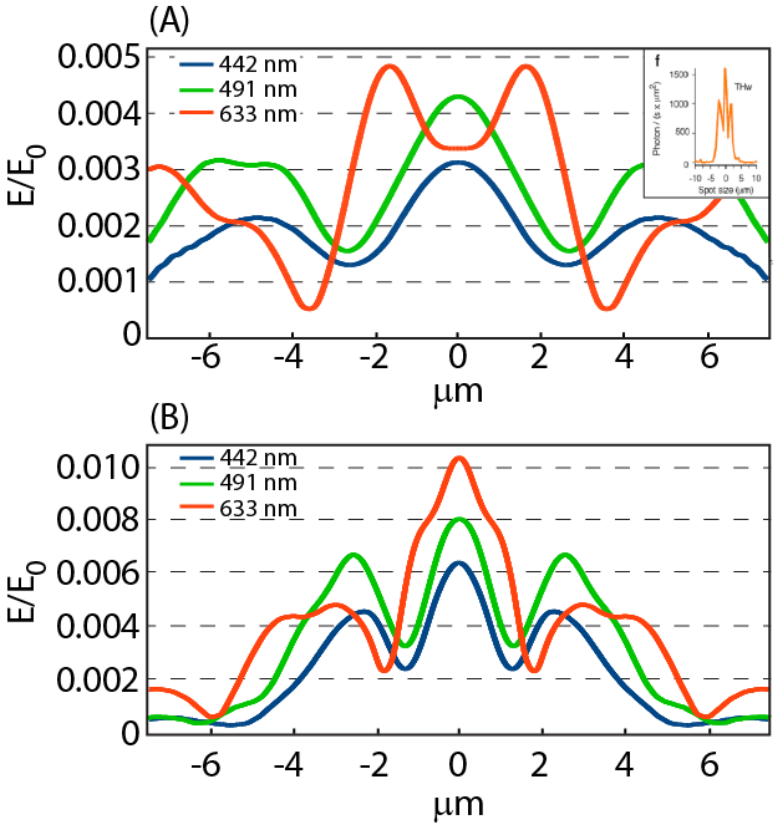

Fig. S4. Simulation of apertureless TOFs: wide Top-hat like (THw) lateral profile. The light profile referred as wide top-hat (THw) shown in Fig. 1F of the main text is characterized by three main peaks, with the middle one slightly dominating over the other two with a width of about 6-9 µm. The numerical simulations show that this profile is obtained by apertureless TOFs with a narrow apex with a total angle of 40 degrees. The agreement of the experimentally measured light profiles and those obtained from numerical simulations is rather remarkable, indicating that the wide top-hat profile is obtained by apertureless TOFs with a narrow conical apex. (A) 1D electric field profile (amplitude E/E_0) calculated at 5 µm from the tip apex. Inset: Fig. 1F in the main text. (B) electric field profile calculated at 2 µm from the tip apex. For both cases an ideal cone with a total apex angle of 40 degrees was chosen. For both (A) and (B) three excitation wavelengths have been considered: 442 nm, 491 nm, 633 nm. Similarly to Fig. S4, for the 633 nm case, there is an off-resonant condition with the fibre geometry.

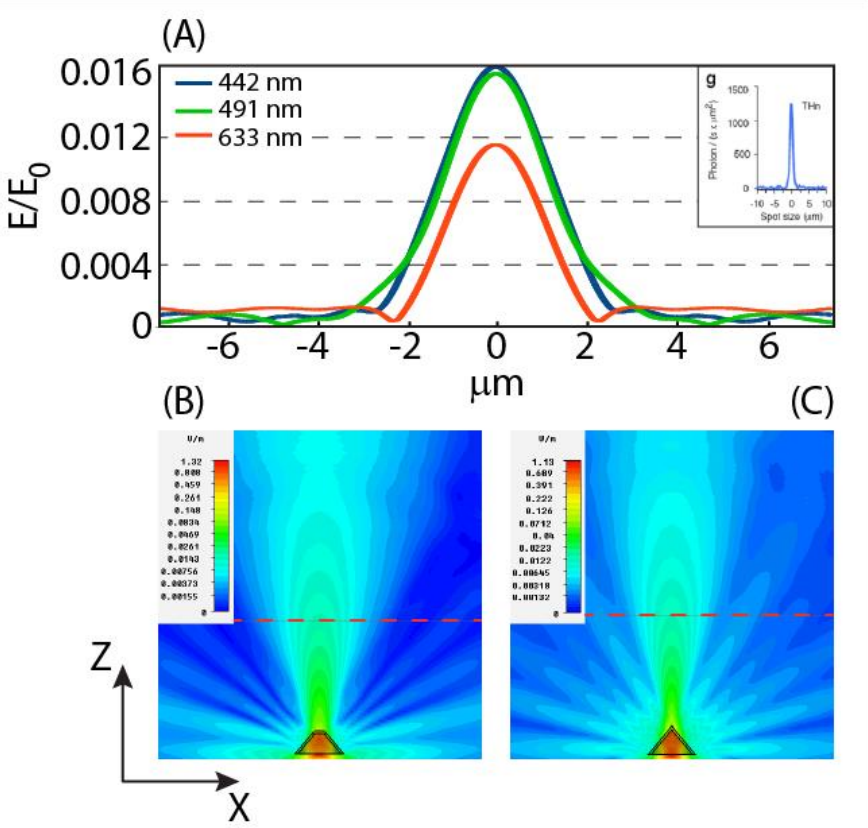

Fig. S5. Simulation of apertureless TOFs: narrow Top-hat like (THn) lateral profile. The light profile of Fig. 1G of the main text referred as a narrow top-hat (THn), has a single lobe. This profile can be obtained from cones with big apex angles, i.e. considering structures geometrically close to standard axicons. In fact, as shown in A, for a total apex angle around 80 degrees, regardless the apex shape, the simulated profile has a single lobe with an average width of 2.8 µm, therefore in the experimental range of 2-5 µm obtained for Fig. 1G. (A) 1D electric field profile (amplitude E/E_0) calculated at 5 µm from the tip apex. A cut-edge cone with an apex angle of 80 degrees was considered together with the three excitations wavelengths, 442 nm, 491 nm and 633 nm. Interestingly, the light profile in all three cases remains almost constant, however a reduction of the light intensity is observed for the 633 nm case. (B) Corresponding 2D distribution in the xz plane. (C) 2D electric field distribution for an ideal cone of 80 degrees total apex angle. The dashed lines represent the 5 µm distance from the cones apex.

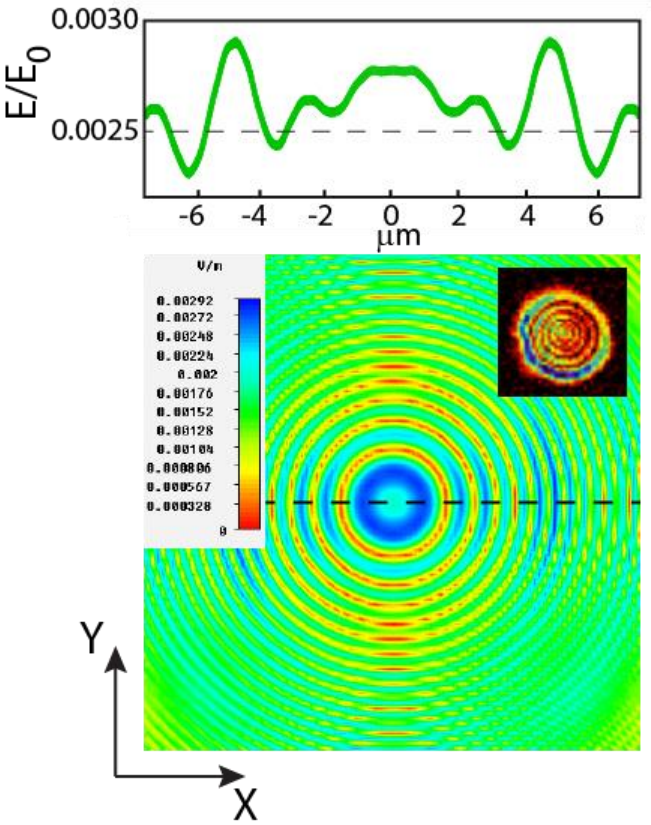

Fig. S6. Simulation of apertureless TOFs: wide Top-hat like (THw) spatial profile. (top) 1D electric field profile (amplitude E/E_0) calculated at about 7 μm from the apex end. (bottom) 2D map of the electric field on the xz plane at about 7 μm from the tip end. The chosen TOF has a cut-edge cone with 40 degrees total apex angle. For better illustrating the almost circular behaviour (the light tends to have a x orientation due to the polarization of the incident light) the specific zero phase component was chosen. The chosen wavelength is 491 nm. Inset: Supplementary Fig. S2K.

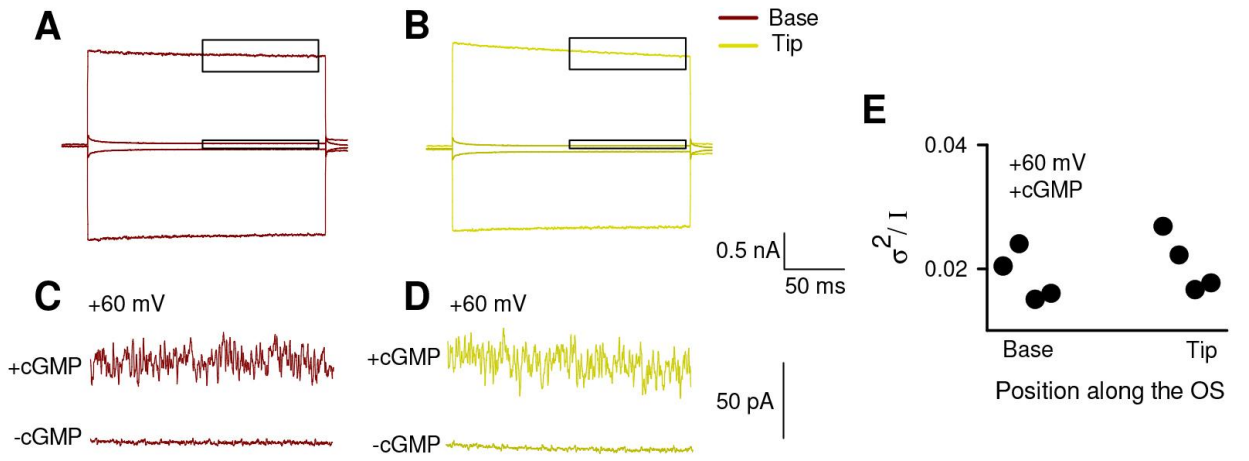

Fig. S7. Patch-clamp recording along the rod OS. (A-B) Macroscopic current recorded (see Ref. 14 for method details) from excised-patches in symmetrical Na^+ before and after the addition of 1 mM cGMP elicited by voltage steps of ±60 mV at the base (A) and tip (B) of rod OS from *Xenopus laevis*. (C-D) Enlargement of macroscopic currents in (A) and (B) (see rectangle for the localization of selected regions) in the presence (+cGMP) and in the absence (-cGMP) of cyclic nucleotide at +60 mV. (E) Plot of the ratio σ^2/I - which is approximately equal to $i_{(sc)}*P_{(closed)}$ - for patches excised at the base (n=4) and at the tip (n=4); σ^2 is the variance of current fluctuations, I is the amplitude of the current, $i_{(sc)}$ is the single channel current and $P_{(closed)}$ is the closure probability. Because the mean±standard deviation is 0.019±0.004 and 0.021±0.005 at the base and tip respectively, it is concluded that the conductance of CNG channels is very similar along the rod OS.

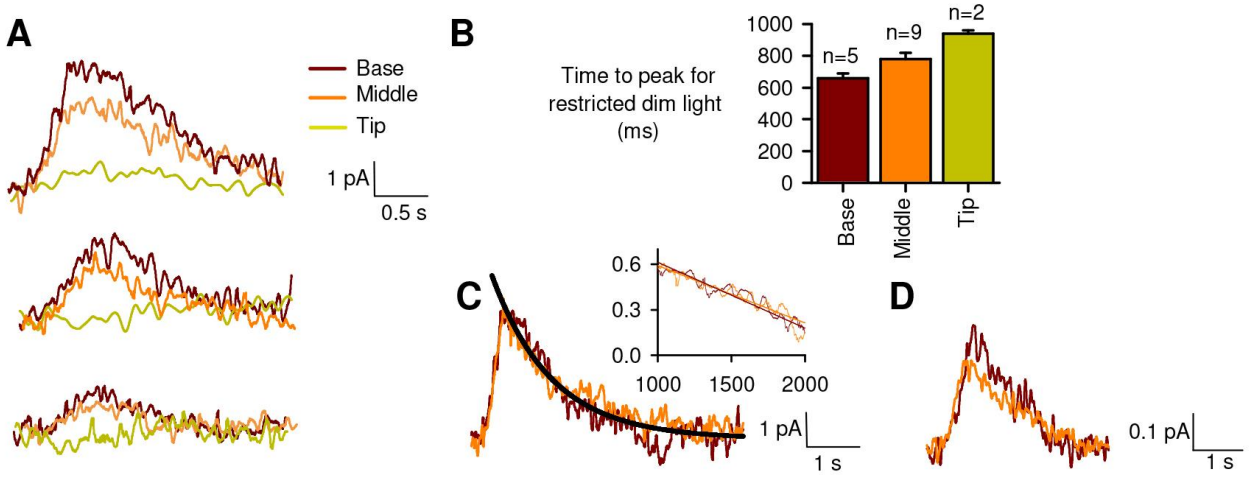

Fig. S8: Comparison of dim flash photoresponses evoked with TOF. (A) Superimposition of photoresponses obtained with dim light intensities (200, 500 and 1000 a.u. bottom, center and top, respectively) evoked at different positions along the rod OS (see color code). (B) Mean time to peak of dim flashes at the base, middle and tip respectively. (C) Superimposition of photoresponses evoked at the base and middle: the light intensity of the flash at the middle (orange) is twice of that used to evoke the photoresponse at the base (red). In black the fit obtained with the following the exponential fit $A(t)=A_0\, e^{-\lambda*t}$. The inset represents the fit of log(A) vs t we used to obtain λ (the slope): the two fits gave identical value of λ, confirming the same kinetics of the falling phase at the base and the middle. (D) Superimposition of mean of single photon responses evoked at the base and middle from the recordings of Fig. 7A-D.

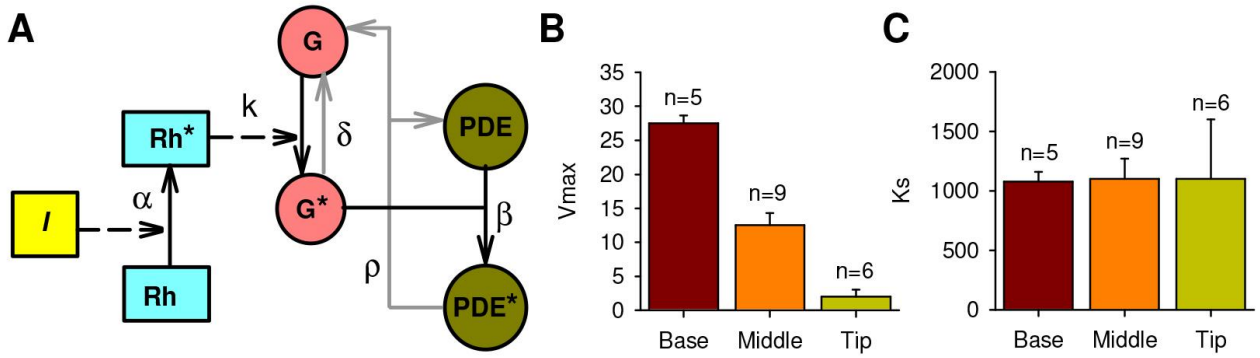

Fig. S9: Model for PDE depletion. (A) Sketch of the first part of the phototransduction cascade which is not affected by the calcium feedback. A gray line denotes a decay process. (B-C) parameter values of Eq. S6 used for the fitting of data in Fig. 4F of the main text.

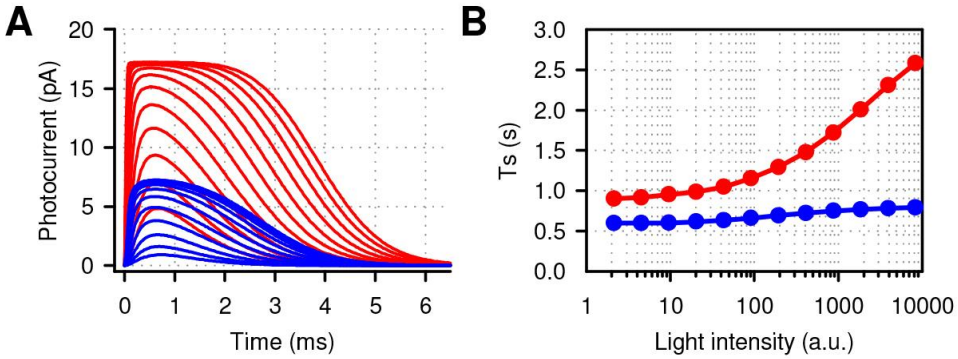

Fig. S10: Model Simulation for saturation time. (A) simulated photocurrents evoked by different light intensities. (B) saturation time vs light intensity. Blue: restricted illumination at the middle of the OS. Red: diffuse illumination. Parameter values of equations (S16) in Supplementary Text: k=40 s^{-1}; ρ=2 s^{-1}; φ=40 μMs^{-1}; η = 2 s^{-1}; K_s=1000 a.u. H = 2 μM; D=40 $\mu m^2/s$ and J=0.16 pA/μm.

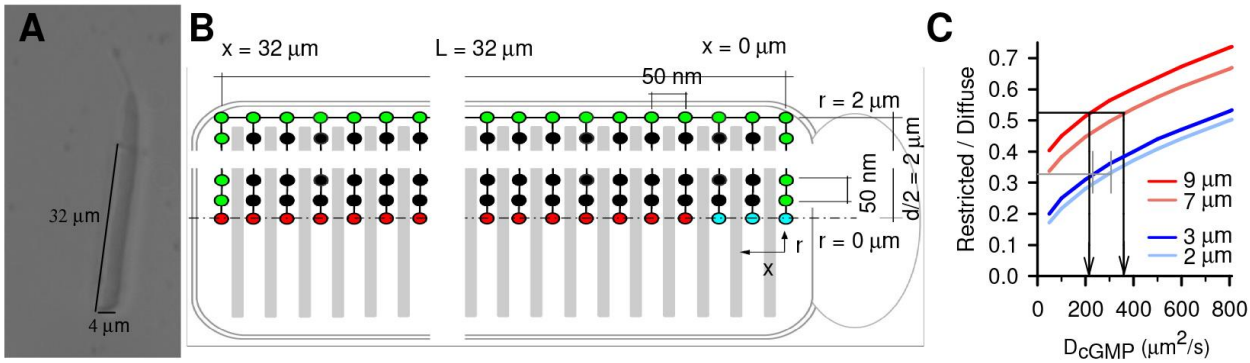

Fig. S11: Model for cGMP diffusion: (A) a DIC image of a rod showing the size of the OS. (B) schematic representation of the grid for the numerical simulations (see text for more details on the colours) (C) Theoretical ratio between restricted and diffuse saturating photoresponses (measured at 500 ms) vs D_{cGMP} in the case of illumination at the base. Red lines: THw fiber (7-9 μm, see Fig. 2C), blue lines: THn fiber (2-3 μm, see Fig. 2B). From the restricted/diffuse ratio equal to 0.52 (THw fiber) and 0.31 (THn fiber), the estimated value of D_{cGMP} varies between 220 and 360 $\mu m^2/s$.